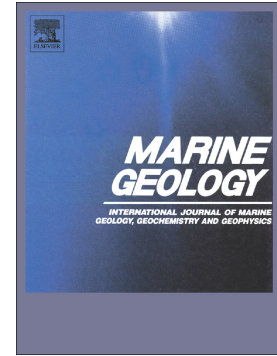


## Journal Pre-proof

Fault-controlled contourite drifts in the southern South China Sea:  
Tectonic, oceanographic, and conceptual implications

Shan Liu, F. Javier Hernández-Molina, Zhenyu Lei, Débora Duarte, Hui Chen, Ce Wang, Yaping Lei, Haiteng Zhuo, Shuqin Huang, Li Zhang, Ming Su



PII: S0025-3227(21)00002-5

DOI: <https://doi.org/10.1016/j.margeo.2021.106420>

Reference: MARGO 106420

To appear in: *Marine Geology*

Received date: 15 September 2020

Revised date: 3 January 2021

Accepted date: 5 January 2021

Please cite this article as: S. Liu, F.J. Hernández-Molina, Z. Lei, et al., Fault-controlled contourite drifts in the southern South China Sea: Tectonic, oceanographic, and conceptual implications, *Marine Geology* (2021), <https://doi.org/10.1016/j.margeo.2021.106420>

This is a PDF file of an article that has undergone enhancements after acceptance, such as the addition of a cover page and metadata, and formatting for readability, but it is not yet the definitive version of record. This version will undergo additional copyediting, typesetting and review before it is published in its final form, but we are providing this version to give early visibility of the article. Please note that, during the production process, errors may be discovered which could affect the content, and all legal disclaimers that apply to the journal pertain.

© 2021 Published by Elsevier.

**Fault-controlled contourite drifts in the southern South China Sea: tectonic, oceanographic, and conceptual implications**

Shan Liu<sup>a, b, 1</sup>, F. Javier Hernández-Molina<sup>c</sup>, Zhenyu Lei<sup>d, 1</sup>, Débora Duarte<sup>c, e</sup>, Hui Chen<sup>a</sup>, Ce Wang<sup>a, b</sup>, Yaping Lei<sup>a</sup>, Haiteng Zhuo<sup>a</sup>, Shuqin Huang<sup>a</sup>, Li Zhang<sup>d</sup>, Ming Su<sup>a, b, f\*</sup>

<sup>a</sup> School of Marine Science, Sun Yat-sen University, Zhuhai, 519083 China

<sup>b</sup> Southern Marine Science and Engineering Guangdong Laboratory (Zhuhai), Zhuhai, 519000, China

<sup>c</sup> Department of Earth Sciences, Royal Holloway University of London, Egham, Surrey TW20 0EX, UK

<sup>d</sup> Guangzhou Marine Geology Survey, China Geological Survey, Ministry of Natural Resources, Guangzhou 510760, China

<sup>e</sup> Marine Geology and Georesources Division, Portuguese Institute for the Sea and Atmosphere (IPMA), 1749-077 Lisbon, Portugal

<sup>f</sup> Guangdong Provincial Key Laboratory of Marine Resources and Coastal Engineering, Guangzhou Guangdong, 510006, China

\* corresponding author.

Tel: + 86-0756-3668556

E-mail address: suming3@mail.sysu.edu.cn (M. Su)

Present address: School of Marine Science, Sun Yat-sen University, Zhuhai, 519083, China.

<sup>1</sup> These authors contributed equally to this work.

**Abstract**

Over the past decades, contourite drifts have been widely identified in the deep ocean with their classification constantly being improved. Some contourite drift types, however, are not yet well constrained. The present study investigates contourite drifts in the southern South China Sea for the first time based on high-resolution reflection seismic profiles and bathymetric data, thereby determining the common occurrence of a lesser-known type: the “fault-controlled drift.” In this area, normal fault movements have been active during the Quaternary, associated with the formation of sea-floor irregularities and highs that represented obstacles to Deep Water circulation. Six fault-controlled drifts are generated in the study area due to interactions between regional faulting/fault-generated topography and bottom currents. They are divided into two major types depending on their shapes, locations, and relative faulting movements: Type-1) drifts deposited coeval to the fault movement and are situated over the footwall block top or along the fault scarp, and Type-2) drifts deposited after the fault movement and are located along the fault scarp base. Spatial distribution of these drifts is a result of variations on bottom currents dynamics associated with the South China Sea Deep Water. The South China Sea Deep Water settling depth, 200-300 m shallower than that of the northern South China Sea, tentatively indicates upwelling which may have, in turn, contributed to the South China Sea meridional overturning circulation. The present study demonstrates new types of contourite drifts that are not well-constrained in the literature and require more detailed studies. The types of fault-controlled drift are described based on the relative movement of normal faults. However, future research should be conducted in other active tectonic settings for evaluating fault effects on the sedimentary stacking patterns, geometries, and evolution of contourite drifts.

**Keywords:** Contourites; Bottom currents; Normal faults; Fault-controlled drifts; The South China Sea Deep Water; The southern South China Sea.

## 1. Introduction

Deep-sea circulation is mainly composed of semi-permanent density-driven circulation (Wunsch, 2002; Kuhlbrodt et al., 2007), also known as bottom currents (Rebesco et al., 2014). Bottom currents tend to flow parallel to large-scale bathymetry (e.g., along the continental margin) or be modified by small-scale topographic features (e.g., seamounts, ridges, straits, mounds, banks) (Preu et al., 2012; Liu et al., 2019). These bottom currents profoundly affect deep-ocean sedimentary processes when the velocity is high enough to transport and erode sediments (Stow et al., 2009; Rebesco et al., 2014). One place where this process occurs is often associated with tectonic-influenced seafloor irregularities in the continental margin (Hernández-Molina et al., 2008a).

Contourites are the sediments deposited or substantially reworked by the persistent action of bottom currents (Rebesco et al., 2014). Contourite drifts are large sedimentary accumulations of contourites (Faugères et al., 1999). Contourite drifts often have a mounded geometry that creates a relief above the seafloor (Miramontes et al., 2019). They are widely observed along continental margins and in deep-sea basins with many shapes, scales, sedimentary patterns, and construction mechanisms (Llave et al., 2019; Mulder et al., 2019). The nature of bottom currents and regional slope geomorphology directly determine the contourite drift types (Hernández-Molina et al., 2008a; Rebesco et al., 2014).

Fault-controlled drifts (FD) were originally included in current-drift classifications by Rebesco (2005) based on previous considerations from Rebesco and Stow (2001) and Stow et al. (2002). These have been identified along steep slopes (Faugères and Stow, 2008) and in abyssal plains (Maldonado et al., 2005; Hernández-Molina et al., 2008b). These drifts can develop either at the base or the top of a fault-generated relief in response to local bottom-current processes variations due to seafloor irregularities (Rebesco et al., 2014). Unlike other well-studied contourite drift types (Faugères et al., 1999; Hernández-Molina et al., 2010), FD and associated fault-contourite interactions are not yet well constrained (Ceramicola et al., 2001; Maldonado et al., 2005). Tectonic considerations on contourite drifts are generally focused on basin-scale tectonics, which can significantly change basin (paleo-) topography, in turn controlling the generation of contourite drifts (Jones and Okada, 2006; Roque et al., 2012; Levchenko et al., 2018). Regional-scale fault movements can particularly be involved in generating FD (Rebesco et al., 2005). Some of the clearest FD evidence was documented in Lake Baikal (Russia) and in the Weddell Sea (Antarctica), where bottom currents significantly interacted with fault-generated seafloor irregularities.

Those drifts have steep flanks and irregular mounded geometries. However, their characterizations and spatial distributions are limited, and the geomorphology and sedimentary patterns of FD remain poorly understood.

In the South China Sea (SCS), the SCS Intermediate Water (IW) and the SCS Deep Water (DW) are responsible for the generation of contourite drifts (Chen et al., 2016; Yin et al., 2019). Erosional, depositional, and mixed features are identified in the northern SCS, with examples of elongated, mounded, and separated drifts (Palamenghi, et al., 2015; Liang et al., 2019; Yin et al., 2019). Intermittent oceanographic processes, such as eddies and internal waves, largely enhance bottom currents and significantly change seafloor geomorphology in the margin- or basin-scale (Yin et al., 2019). While IW- and DW-related contourite drifts are widely explored in the northern SCS, southern SCS contourite features have not been investigated. Southern SCS seafloor morphology is largely affected by tectonics (Hutchison, 2004), thereby determining a complex margin morphology, including seamounts, small-scale structural highs, and fault-generated basement reliefs (Zhang et al., 2003). These complex seafloor irregularities provide an opportunity to examine interactions between fault-generated topography and oceanographic processes.

The present study aims to describe in detail the interacting process and present first-time southern SCS FD. Therefore, the objectives of the present study are a) indicate the spatial distribution and geomorphology of southern SCS FD; b) discuss interactions between bottom-current processes, gravity flows, and faulting movements; and c) provide new insights into the fault-controlled drift conceptual model.

## **2. Regional setting**

### **2.1 Geological settings**

The SCS is the largest marginal sea in the western Pacific Ocean. The Beikang basin, also known as the Sarawak Basin (Madon et al., 2013), is located at the southern SCS between a water depth of 200 m and 2275 m (Fig. 1). It is bounded by Nanwei Bank and Nansha Islands to the north and the continental shelf to the south (Fig.1b). Parts of the Nawei basin, the Nanwei continental slope, and the Nansha Trough are the northwest, southwest, and southeast components of the study area (Fig. 1b). The rest of the study area consists of the majority of the Beikang basin (Fig. 2).

The SCS opening was initiated at ~33-30 Ma and sedimentary basins in the study area began forming (Sibuet et al., 2016). NE-SW orientated dextral strike-slip tectonics largely affected the evolution of these sedimentary basins, resulting in several NE-SW, NW-SE, and N-S orientated normal faults in the Beikang basin during the Oligocene (Zhang et al., 2003). Subsequently, regional compression uplifted the Beikang basin and faulting activities were enhanced in the study area (Madon et al., 2013). Large-scale tectonics gradually ceased in the southern SCS during the early Miocene (Hutchison, 2004; Madon et al., 2013). The resulted Early Miocene Unconformity (EMU) separated the pre-Oligocene to the Miocene deformed basement from overlying sedimentary sections (Madon et al., 2013). The southern SCS went into a regional quiescence stage and regional subsidence occurred from the late Miocene (~10.5 Ma) onward (Hutchison, 2004; Madon et al., 2013). The study area gradually became a deeper sedimentary environment with local tectonic activity from the late Miocene to the Quaternary (Zhang et al., 2003).

## 2.2 Oceanographic settings

The semi-enclosed SCS is connected to the western Pacific Ocean through a single deep passage: the Luzon Strait (Fig. 3a). At present, the SCS Surface (SW), Intermediate (IW), Deep (DW), and Bottom (BW) waters are observed from the surface to the sea bottom (Figs. 1, 3b) (Tian et al., 2006). The SW is present from 0 and 500 m water depth (Qu et al., 2006). Its flowing pattern (e.g., directions, strength) is influenced by seasonal monsoon winds and the Kuroshio Current sourced from the NW Pacific (Su, 2004). The IW, sourced from the North Pacific Intermediate Water (NPIW), circulates between a water depth of 500 and 1500 m in an anticyclonic pattern in the SCS (Tian et al., 2006). A baroclinic pressure gradient driving the North Pacific Deep Water (NPDW) into the SCS is observed below a water depth of 1500 m (Qu et al., 2006). The result is that DW flows in a cyclonic pattern between a water depth of 1500 and 2000 m in the SCS (Qu et al., 2006). The BW is a deep-water overflow transported through the Luzon Strait into the SCS (Zhou et al., 2017). It moves below a water depth of 2000 m in a cyclonic flowing pattern (Fig. 1) (Tian et al., 2006).

Present-day oceanographic observations are mainly conducted in the northern SCS, while numerical modelling and simulations are utilized to understand the southern SCS oceanography (Wang et al., 2016). Tidal and eddy-induced mixing processes intensify deep southern SCS circulations. The velocity of related background currents that exist at 2000 m (Fig. 3a) are estimated at 1-5 cm/s (Xiao et al., 2013). Simulations show that oceanic currents gain velocity when encountering southern SCS topographic

features with steep slopes (Xiao et al., 2013). Results derived from the most recent observation fit these simulations and models (Shu et al., 2016). Bottom currents are enhanced by internal tides below 1400 m at the northwest part of Nansha Islands (Shu et al., 2016). Bottom current velocities regionally accelerate to ~10 cm/s by internal tides, which is one order of magnitude greater than the background currents (Shu et al., 2016). In the study area, few studies discussed the present-day ocean circulation patterns. Oceanographic data from the World Ocean Database 2013 (WOD13) indicates the DW presence in the Beikang basin between a water depth of 700 and 1700 m (Figs. 3c, d). The core varies between a water depth of 1300 and 1500 m with a maximum salinity of approximately 34.75 (Fig. 3d).

### 3. Materials and methods

The present study is based on high-resolution multibeam bathymetric, multichannel seismic, borehole, surface sediment cores, and oceanographic data (Fig. 4a). Bathymetric and seismic datasets were obtained during the R/V Tanbao cruise via the Guangzhou Marine Geological Survey in May 1996. Bathymetric data (Figs. 2, 4a) were collected via a Seafloor 2112 multibeam bathymetry system. This system operated at a centre frequency of 12 kHz with a swath width of 120 degrees. Basic parameters of morphological units (e.g., water depth, size, trend, and relief) were measured and analyzed from the bathymetric data. Contourite drift identifications are based on their morphology, geometry, and locations (Faugères et al., 1999; Faugères and Stow, 2008; Rebesco and Stow, 2001; Rebesco, 2005; Rebesco et al., 2014). Isolated mounded features and large-scale alongslope elongation were the main identification elements for distinguishing contourite drifts from canyon-levee systems (Rebesco, 2005; Rebesco et al., 2014). Fault mapping was derived from previous studies (Zhang et al., 2013). Fault-controlled drifts (FD) were identified based on the direct influence of faulting on their location and growth nature (Rebesco, 2005).

Multichannel airgun reflection lines are orientated in NNE-SSW and WNW-ESE directions with an average line spacing of 6 km. The seismic source was located at a depth of 6 m with a short interval of 7 s. The dominant frequency ranged from 40 to 60 Hz. The receiver system with 180 hydrophones was about 2.3 km long. The data were processed by applying pre-stack time migration, denoising, deconvolution, amplitude correction, wavelet coherence, trace select, normal moveout, and multiple wave suppression. The stratigraphic division for major depositional units is based on the identification of regional unconformities (Fig. 3). Two criteria are used for the recognition of seismic units. The first uses local

erosional discontinuity (T3) to separate unit3 from the basement. The other criterion uses a vertical variation of acoustic facies to identify unconformities T2 and T1, and to separate units 2 and 1. The amplitude, internal seismic facies, reflection terminations, and geometry are used to determine the depositional environment in each unit. Moderate-high amplitude, oblique to subparallel reflections with onlap terminations and mounded geometry are seismic characteristics to identify contourite drifts. Low-moderate amplitude and transparent to chaotic reflections represent mass-transport deposits. Moderate-high amplitude and subparallel to parallel reflections are used to recognize pelagic/hemipelagic deposits (Table 1). Major seismic unconformities are correlated with the regional chronological framework derived from the oil well Bako-1. The well was drilled in 1995 by Mobil and the depth reached at 1152 m. The lithology of the well is characterized by a profound hiatus, the early Miocene unconformity (EMU; ~16 Ma) (Madon et al., 2013).

Surface sediment cores were acquired using box corer during the R/V Kexue Yihao cruise via the Chinese Academy of Sciences in April 2012 (Zhang et al., 2016). Box corer sampling stations have an average spacing of 30 km (Fig. 4a). Vertical depth of these surface sediment cores is ~5 cm. Organic matters, carbonate and silica were removed using 15% H<sub>2</sub>O<sub>2</sub>, 0.25 mol/L HCL, and 2 mol/L Na<sub>2</sub>CO<sub>3</sub>, respectively. Grain size analysis was performed at the Institute of Oceanology, Chinese Academy of Sciences using a laser diffraction particle size analyzer Cilas 940L. This device measured a grain size range of 0.3 to 2000  $\mu$ m with analytical precision better than 2%. Mean grain size and sorting are calculated using the method of McManus (1988). Udden–Wentworth ( $\phi$ ) grain size scale (Wentworth et al., 1922) is applied. Results are compared using cross-plots (Folk, 1964; Martins, 2003).

Vertical CTD profiles were extracted from the World Ocean Database (2013). The salinity cross-section (Fig. 3d) was made utilizing the Ocean Data View (ODV) software. These data were utilized to identify the regional structure of water masses in the study area and determine the bottom current characteristics interacting with sea-floor irregularities.

## 4. Results & Interpretation

### 4.1 Regional physiographic domains

The study area is divided into several physiographic domains (Fig. 5a). The continental slope is separated into the upper (180-1000 m water depth), middle (1000-2000 m water depth), and lower (>



2000 m) slope regions. The upper slope has a slope gradient of  $0.8^{\circ}$ - $5^{\circ}$ . The middle slope has a slope of approximately  $1^{\circ}$ , but can locally reach  $8^{\circ}$ - $30^{\circ}$  with faults generating topography (Fig. 5b). The lower slope displays a gentle slope gradient of  $0.1^{\circ}$ - $0.8^{\circ}$ . The middle slope is the main morphological component of the study area, consisting of mass-transport deposits (MTD) in the southwest part (Fig. 5a, Table 1). Submarine canyon systems and alongslope features are mainly distributed in the western part (Fig. 5a). Several structural highs with area ranging between 5 and 35 km<sup>2</sup> are located in the middle and the lower slopes and their flanks have a slope gradient of  $9^{\circ}$ - $28^{\circ}$  (Fig. 5b).

#### 4.2 Main seismic units

Three seismic units (Units 3, 2, and 1 from bottom to top) bounded by major discontinuities (T3, T2, T1) have each been identified from old to young (Figs. 4b, c). T3, T2, and T1 are unconformities with high-amplitude reflections. Below these units, the basement is characterized by medium-high amplitude and chaotic and discontinuous reflections (Figs. 6, 7, 8).

Seismic unit 3 is characterized by high amplitude and disrupted/semi-continuous chaotic-subparallel reflections. It is separated from the basement by a discontinuity T3 (Fig. 4b). Low-angle onlap terminations toward the fault-generated reliefs are observed at the base of this unit at the central part of the basin (Figs. 6a, c). This unit has a maximum sedimentary thickness of 1 s TWT at the northern part of the basin (Fig. 8f), but the thickness varies between 0.3 s and 0.5 s TWT at the rest of the basin.

Seismic unit 2 is bounded by discontinuity T2 at its base. It consists of high amplitude and continuous subparallel reflections (Figs. 6, 7). High-angle downlap, onlap, and truncated terminations are recognized on the fault plane at the central part of the basin (Fig. 6). The sedimentary thickness of unit 2 is relatively constant (about 0.2 s TWT), but locally it reaches 0.5 s TWT between the tectonic deformed areas at the northern part of the basin (Figs. 6b, c).

Seismic unit 1 is bounded by discontinuity T1 at the base and by the seafloor at its top. It is internally characterized by moderate-high amplitude and continuous oblique-subparallel reflections. It is identified via reflections terminations with low-angle onlap and downlap terminations toward T1 and high-angle onlap terminations onto the fault plane (Fig. 7c).

### 4.3 Morphological features

#### 4.3.1 Contourite depositional features

Mounded features with moderate-high amplitude, oblique to subparallel reflections with onlap terminations in unit 1 are interpreted as contourite drifts based on the geometry and internal seismic facies. Among these drifts, fault-controlled drifts (FD) are identified based on the direct influence of faulting on their location and growth nature, while an elongated and mounded drift (MD) is recognized based on the mounded relief and the external shape.

Six FD are identified in the study area (Fig. 5a, Table 2). Fault-controlled drift 1 (FD-1) is located at a depth of 1470-1910 m and associated with an NNW-dipping and a W-W-E-NE orientated normal fault (Fig. 5a). This drift slope gradient varies from 7° to 13° (Fig. 5b). The drift encompasses an area of 21 km<sup>2</sup> and is approximately 12 km long and 1-2.5 km wide. Slightly mounded geometry, moderate to high amplitude, and sigmoid to parallel reflections with onlap terminations are observed at the hanging wall block (Fig. 6a). Moderate to high amplitude and parallel reflections with onlap and downlap terminations are shown at the footwall block of the fault (Fig. 6a). The sedimentary thickness of FD-1 was about 0.2-0.7 s TWT.

The fault-controlled drift 2 (FD-2) is associated with the same normal fault as FD-1 (Fig. 5a). It is located at a depth of 1290-1660 m (Fig. 5a). The slope gradient steepens to 14°-28° from the southwest to the northeast (Fig. 5b). This drift has a length of 16 km and a width of 2-3 km, covering an area of 40 km<sup>2</sup>. Irregularly mounded geometry and moderate to high amplitude, chaotic to sigmoid reflections with onlap, as well as downlap and truncated terminations are shown at the fault footwall area (Figs. 6b, c). The sedimentary thickness of FD-2 varies between 0.5 s and 1.1 s TWT (Figs. 6b, c).

The fault-controlled drift 3 (FD-3), associated with a NE-dipping, NW-SE orientated normal fault, is located between a water depth of 1230 m and 1480 m (Fig. 5a). The drift has a slope gradient of approximately 7°-15°. It covers 74 km<sup>2</sup>. The length is approximately 14 km and the width is 5-6 km (Fig. 5a). Moderate to high amplitude and sigmoid to mounded reflections with onlap terminations are identified at the hanging wall area, while parallel reflections with onlap terminations are displayed at the fault footwall area (Fig. 7a). The sedimentary thickness of this drift varies between 0.3 s and 0.5 s TWT.

The fault-controlled drift 4 (FD-4) lies between a water depth of 1420 m and 1810 m. It is associated with an SW-dipping, NW-SE orientated normal fault (Fig. 5a). The slope gradient is approximately 9°-17°

(Figs. 5a, 7b). This drift has a length of approximately 19 km and a width of 4-7 km. It encompasses an area of 107 km<sup>2</sup> (Fig. 5a). The hanging wall area of the fault mounded geometry is identified by moderate to high amplitude and sigmoid to mounded reflections with onlap terminations (Figs. 7b, 7c). Moderate to high amplitude, parallel reflections with onlap, and downlap terminations are observed at the fault footwall area (Figs. 7b, 7c). The sedimentary thickness of FD-4 is approximately 0.3-0.5 s TWT.

The fault-controlled drift (FD-5) is associated with an NW-dipping, NE-SW orientated normal fault (Fig. 5a). It is located at a depth of 1380-2040 m (Fig. 5a). The drift encompasses an area of 32 km<sup>2</sup> and is approximately 4 km long and 4-9 km wide (Fig. 5a). The slope gradient is approximately 6°-10° (Fig. 5b). Slightly mounded geometry, moderate amplitude, and sigmoid-mounded to transparent reflections with onlap terminations are identified at the hanging wall area, while moderate to high amplitude, parallel reflections with onlap, and downlap terminations are shown at the fault footwall area (Fig. 8c). The sedimentary thickness of FD-5 varies between 0.1 s and 0.6 s TWT (Fig. 8c).

The fault-controlled drift (FD-6) is associated with the same fault as FD-5. It is located between a water depth of 1190 m and 1630 m. The slope gradient increases from 15° to 28° toward the northeast (Fig. 5b). This drift has a length of 16 km and a width of 1-3 km, covering an area of 40 km<sup>2</sup> (Fig. 5a). At the fault footwall area, the mounded shape is recognized with moderate amplitude, sigmoid to parallel reflections with onlap, and downlap terminations (Fig. 8b). The FD-6 sedimentary thickness varies from 0.5 s and 0.9 s TWT.

In addition to fault-controlled drifts, an NW-SE orientated MD is identified adjacent to FD-1 and FD-6 with a slope gradient of 25-35° (Fig. 5a). This drift is located at a depth of 1390-1650 m. This drift with mounded geometry has moderate to high amplitude sigmoid to parallel reflections with onlap and downlap terminations (Fig. 8d). The sedimentary thickness of this mounded drift varies between 0.3 s and 0.5 s TWT. However, only one seismic line has crossed this drift and its orientation is not perpendicular to the mounded relief. The mounded internal feature is not as typical as those observed in other regions (Hernández-Molina et al., 2014). More data are needed to confirm the interpretation of this MD.

#### 4.3.2 Contourite erosional features

U-shaped incisions associated with contourite drifts in seismic unit 1 are interpreted as non-depositional/erosional moats. An NW-SE orientated moat is observed associating with FD-3 at the northeast part of the basin (Fig. 7a). It has an asymmetric U-shaped profile extending between a water depth of 1440 m and 1510 m. The moat narrows toward the southwest and the width decreases from 1.6 to 0.8 km. The incision depth of this moat varies from 50 to 90 m.

At the central part of the study area, an NW-SE trending moat is associated with FD-4 (Figs. 7b, 7c). The moat is located between a water depth of 1480 m and 1510 m and has an asymmetric U-shaped profile (Figs. 7b, 7c) with an incision of approximately 70-90 m. The moat width narrows from 0.6 to 0.34 km from the southeast to the northwest.

Another NW-SE trending moat is associated with the MD (Fig. 8d). It has a V-shaped profile and is located between a water depth of 1500 m and 1530 m. The width ranges from 0.6 to 1.2 km and the depth varies from 20 to 60 m. The moat narrows to a minimum width toward the southwest.

#### 4.3.3 Gravitational features

A group of slope-confined canyons is presented on the slope adjacent to the FD-6 (Figs. 5a, 8a). These canyons are observed in seismic unit 1. They are distributed in a WNW-ESE orientation and extend downslope from a water depth of 1100-1320 m to 2000-2200 m (Fig. 8a). Their width varies between 0.5 km and 0.7 km and the length ranges from 4.3 km to 6 km. The average slope gradient of the canyon axes decreases downslope from the canyon heads ( $21^\circ$  slope) to the canyon mouths ( $4^\circ$  slope). Most of the canyons display distributary channels that gradually merged in the middle slope (Fig. 8a). Steep sidewalls with slopes of  $13^\circ$  to  $22^\circ$  are shown in these canyons. Southwest sidewalls ( $18^\circ$ - $22^\circ$  slope) are steeper in comparison to those in the northeast ( $13^\circ$ - $20^\circ$  slope).

Another canyon system is observed northwest of FD-6 (Fig. 5a). These canyons extend downslope in an NNE-SSW direction from a water depth of 1100-1320 m to 2000-2200 m. They have a width of 0.3-0.6 km and a length of 1.5-3 km. The average canyon axes slope gradient decreases downslope from  $28^\circ$  to  $9^\circ$  (Fig. 5b). No distributary channels are shown in these canyons (Fig. 5a). Southwest sidewalls with a slope of  $10^\circ$ - $20^\circ$  slope are gentler than those in the northeast ( $18^\circ$ - $28^\circ$  slope).

Inter-canyon sedimentary ridges are displayed between the canyons (Figs. 8b, e). Their dimension increases toward the southwest from 1.5-3 km<sup>2</sup> to 7-8.5 km<sup>2</sup>. They have an average thickness of approximately 0.3 s TWT. These sedimentary ridges display mounded geometry and moderate to high amplitude, as well as chaotic to parallel reflections (Figs. 8b, e). Onlap and downlap terminations are observed onto discontinuity T3, while truncations are identified at the canyon sidewalls (Fig. 8e). Also, channel infill features are recognized within inter-canyon sedimentary ridges. These features are characterized by high amplitude chaotic reflections (Fig. 3). Mass-transport deposits (MTD) with low-moderate amplitude, transparent to chaotic reflections are observed at the base of these Inter-canyon sedimentary ridges. Their size and scale can hardly be calculated due to the limited spatial distribution of the seismic data.

## 5. Discussion

### 5.1 Chronostratigraphic framework

Major seismic unconformities included T3, T2, and T1 (from bottom to top) are correlated with the regional chronological framework provided by Madon et al. (2013) (Fig. 4c). Borehole Bako-1, the only well in the Beikang basin, recovered sediments with an Oligocene-middle Miocene age (Fig. 4c). The early Miocene unconformity (EMU; ~16 Ma) from this well was tied to seismic data by previous studies. The EMU is about 2.9 s TWT deep at the location of Borehole Bako-1 (Madon et al., 2013). This erosional discontinuity, a significant hiatus related to the end of active rifting (Hutchison, 2004), is tentatively correlated with T3 by this study through connecting seismic profiles (Fig. 4c). As such, T3 could be considered as the early Miocene unconformity.

Madon et al. (2013) correlated the Pliocene and Quaternary seismic units with data derived from onshore wells. The Base-Pliocene unconformity (~5.5 Ma) significantly separated the underlying fault-influenced and overlying subparallel seismic units. This unconformity is coeval with the cessation of regional tectonics. A similar seismic feature is observed in units 3 and 2 of this study, suggesting similar time intervals. The Quaternary unconformity (~2 Ma) marked a seismic facies transition from subparallel to oblique-chaotic, which is similar with the seismic characteristics of units 2 and 1 of this study. These regional discontinuities from their study are correlated with T2 and T1 from this study by connecting seismic profiles (Fig. 4c). Therefore, T2 is considered as the base of the Pliocene and T1 is attributed to an early Quaternary age.

## 5.2 Decoding processes from morphological features

### 5.2.1 Tectonic implications

Most faults only extended from the base towards discontinuity T2 (Fig. 8c), indicating the cessation of regional tectonic activity since the middle Miocene in the study area. The end of large-scale tectonics (e.g. Sabah Orogeny, seafloor spreading) was dated to the early to middle Miocene in the southern SCS (Hutchison, 2004; Cullen, 2010). The Beikang basin subsequently went into a tectonic quiescence stage (Madon et al., 2013). Some faults, however, extended from units 3 to 1 and nearly reached the seafloor (Fig. 7), indicating a possible reactivation of previous faulting movements during the Quaternary.

Fault-controlled drifts (FD) and associated erosional features (rills) are conditioned via sea-floor irregularities or highs due to reactive fault movements at the central and northeast parts of the study area. Plenty of faults are shown at the western and southern parts of the basin as well (Fig. 5a). However, the associated faulting movement did not sufficiently create irregularities or highs on the seafloor. The distribution of FD, therefore, is possibly influenced by the fault-generated topography. Also, these locations are dominated by the gravity process which is evidenced by the widely distributed MTD. The depth of these locations is relatively shallower (200-1000 m) than the settling depth of the South China Sea Deep Water (DW). As such, the fault-generated topography, dominated sedimentary process, and settling depth of the deep water can be controlling factors for the distribution of FD.

The relative continuous or intermittent fault activity plays a significant role in controlling the final drift geometry (Figs. 6a, 7, 8c). The geometry and internal structure of FD-3 and FD-4 are both similar to the infill drifts (Fig. 7) (Labesco, 2005; Rebesco et al., 2014), which are sometimes deposited via the bottom current action within the scarp formed by mass-transport processes, such as slumps or slides (Solheim et al., 2005; Laberg and Camerlenghi, 2008). Both FD-3 and FD-4 display onlap and downlap seismic terminations toward the previously fault-generated scarp (Fig. 7). Reflections here are ending abruptly against the fault planes, and they are not changing its inclinations or being distorted. Therefore, FD-3 and FD-4 are linked to normal faults with instantaneous movements and sedimentary depositional processes that occurred after the fault movement.

In contrast, the FD-1 and FD-6 depositions have been occurring coevally with the continuous fault movement and growth. Reflection terminations change its inclinations and are distorted toward the fault

plane and the footwall block basement (Figs. 6a, 8c). Slightly mounded features are observed over the fault plane top. Similar seismic facies have been identified on contouritic drifts in Lake Baikal (Russia) where active faulting has been continuously affecting drift developments (Ceramicola et al., 2001).

Faulting movements associated with FD-2 and FD-5 are difficult to determine. However, FD-1 and FD-2, as well as FD-5 and FD-6, are generated along the same normal faults (Fig. 5a). The FD-2 and FD-5 developments should have been influenced by the synchronous interplay of bottom currents and continuous faulting, just like the other drifts, resulting in irregular mounded geometry within the drifts.

Previous studies have interpreted normal fault occurrence in the study area as resulting from a regional strike-slip tectonic setting during the Miocene (Zhang et al., 2003). These authors, as well as Madon et al. (2013), reported that tectonic activity has been relatively weak or even ceased during the Quaternary. Nevertheless, the present study indicates that at least some local faulting movement occurred during the Quaternary.

#### 5.2.2 Oceanographic implications

The identified contourite features within unit 1 are located within the DW depth range, indicating that the DW was active in the southern SCS since T1 (early Quaternary, ~2 Ma). During the late Pliocene (~3 Ma), the establishment of the modern morphology of the Luzon Strait gradually initiated the modern DW circulation in the SCS (Tian et al., 2017). The narrowing of seaways between the SCS and the Pacific Ocean induced enhanced bottom currents, thereby triggering the southward DW penetration (Tian et al., 2017).

Depositional and erosional contourite feature distributions in the study area reflected the local DW bottom-current dynamics (e.g., flowing depth, velocity, directions). The location of moats, between a water depth of 1440 m and 1530 m, suggested the DW core settling depth in the southern SCS. Moats were formed as a result of non-depositional or locally erosional bottom-current processes due to the action of the core of a dynamic water mass (Rebesco et al., 2014; Mulder et al., 2019). Bottom currents are more intensive and focused on a long-term mean velocity of at least 50 cm/s within moats (Stow et al., 2009; Hernández-Molina et al., 2014; García et al., 2016).

Xiao et al. (2013) and Xie et al. (2013) constructed the SCS deep circulation based on observations and high-resolution simulations. Influences of intermittent processes, such as internal tide and eddy, were considered in their oceanic models. Their models showed a close relationship between the bottom

circulation and the seafloor topography. The average background current velocity associated with the DW was calculated as  $\sim 7$  cm/s in the southern SCS (Fig. 3a). The presence of seamounts or structure highs, however, can cause an acceleration of at least 10 cm/s of bottom current velocity based on their oceanic models. In the study area, the seafloor topography is complex with the presence of the large-scale Nanwei Bank and small-scale structural highs/seamounts (Figs. 1, 2, 4a). Current velocity intensification is possible due to these seafloor features, as it has been proposed in other continental margins and adjacent abyssal plains (Zhang et al., 2016; Liu et al., 2019). Bottom currents can gain velocity ( $\sim 15$  cm/s) by the influence of a kilometre-scale seafloor elevation (Turnewitsch et al., 2004). Also, other secondary oceanographic processes, such as deep tides or internal waves, could modulate and largely enhance local bottom current velocities (Stow et al., 2013; Yin et al., 2019). Therefore, the moat formation in the study area results from the local bottom current enhancements.

Moreover, local spatial grain size variations and silt contents evidenced by Zhang et al. (2016) were indicating local bottom current dynamics in the study area (Fig. 9). The silt content increased by  $\sim 10\%$  and the clay content decreased by  $\sim 12\%$  in the area where the FD-1 was located (east of  $112.5^\circ$  E,  $7.2^\circ$  N) (Fig. 9). These sedimentary variations were unlikely to be influenced by turbidity currents since the submarine canyons were located further east at  $7.4^\circ$ - $7.5^\circ$  N (Fig. 5a) and no significant changes of grain size and silt content were observed (Fig. 9). Coarser grain sizes indicate a stronger bottom current at the seafloor in the drift area. The generation of these contourite drifts initiated since the early Quaternary. Therefore, a local enhancement of current velocities may have taken place already at the time when drift growth started.

The relatively large contourite drift distribution regarding the adjacent moats is related to topographic obstacles, allowing for the decoding of the bottom current directions (Turnewitsch et al., 2013). In the northern hemisphere, the Coriolis force deflects bottom currents to the right, where erosional features generally form, and at the left of the moat, the drifts are laterally deposited under weaker energetic conditions (Faugères and Stow, 2008; Rebesco et al., 2014). In the study area, the distribution of the MD and its adjacent moat, as well as the FD-3, indicate a long-term southwest-directed bottom current (Figs. 5a, 7a, 8a). The FD-4 spatial distribution and the associated moat (in Figs. 7b, c) suggest locally long-term northwest-directed bottom currents (Fig. 5a).



The DW has a shallower flowing depth in the southern SCS when compared to the northern SCS. The interface between the DW and the overlying intermediate water (IW) is located at a water depth of ~1500 m in the northern SCS (Yin et al., 2019), and DW associated contourite features are observed between a water depth of 1700-2000 m (Chen et al., 2016). In the study area, bottom-current circulations derived from the sedimentary record indicate a DW flow, which is 200-300 m shallower than that of the northern SCS. This difference in the DW flowing depth is most likely induced by DW upwelling in the southern SCS.

The Luzon Strait, the deep central SCS basin, and the continental slope of the southern SCS are the proximal, intermediate, and distal sites of the DW, respectively (Shu et al., 2014). After passing its source area, diapycnal mixing between the DW and other layered water masses are promoted via internal tides. Mixing processes were further intensified due to complex seafloor topography when the DW flows to its intermediate site (Tian et al, 2006; Cai et al., 2020). When the DW moves southward and reaches Nansha Islands (in Fig. 1b), the slope-trapped waves and Rossby waves trigger the water mass upwellings (Shu et al., 2016; Wang et al., 2016). Mixing processes together with complex seafloor topography induces the SCS meridional overturning circulation (MOC), which upraise deep waters in the southern SCS and transport the DW back northward to the northern SCS (Wang et al., 2016). Previous studies discussed the structure and pattern of SCSMOC mainly based on simulation and oceanic models. Results from the present study evidently indicate that DW upwelling occurred at the southernmost deep setting of the SCS based on the sedimentary record.

### 5.2.3 Interactions between bottom currents and gravity flows

Submarine canyon systems along the slopes of local highs indicate the gravity flow action (Figs. 8a, e). In the study area, inter-canyon sedimentary ridges with asymmetric flanks are shown at the middle-reach canyon (Figs. 8b, e). Their progradational pattern and NW-trend channel migration are in the reverse direction of the estimated bottom currents (Fig. 8e). These features are comparable to that defined mixed system that resulted from interplay between downslope gravity flows and the alongslope bottom current along the East African margins (Sansom, 2018; Fonnesu et al., 2020), or the investigated lab experiments (Miramontes et al., 2020). However, canyons with mixed features from these previous studies are located close to the continental shelf where the sediment supply is adequate. Significant flow-stripping and deviation of turbulent, fine-grained suspension clouds occurred when bottom currents interacted with

turbidity currents at those locations (Fonnesu et al., 2020). In the study area, observed canyon systems have a profound distance from the shelf (Fig. 5a), indicating different interacted processes compared to the above-mentioned examples.

The canyon foot shows mass-transport deposits (MTD) at the seismic scale (Fig. 8b). The presence of MTD is most likely induced by slope failure. Both canyon systems in the study area are associated with steep fault-generated slope (Fig. 5a). Slope gradients generally reach  $21^\circ$  at the canyon head (Fig. 5b). These morphologic features are similar with those observed in a slope-confined canyon system offshore New Jersey, US (Dugan et al., 2000; Mchugh et al., 2002). Pratson and Coakley (1996) investigated the slope gradient threshold triggered slope failure and the formation of this canyon system using simulations. Their study demonstrated that a steep slope with a slope gradient of  $12^\circ$ - $30^\circ$  can significantly induce gravitational collapse. The resulted slope failure can evolve into a slope-confined canyon depending on sediment inputs (Pratson and Coakley, 1995). As such, canyon systems of this study possibly have similar formation mechanism. Sedimentary accumulation of contourite drifts provides sufficient sediment input and gravitational collapse of the steep fault scarp forms the canyon systems in the study area.

### 5.3 Fault-controlled drifts: types and sedimentary model

The most recent contourite drift classifications define that fault-controlled drifts were either generated at the base or top of a fault-generated basement relief (Rebesco et al., 2014). In the southern SCS, fault-controlled drifts are associated with normal faults, and two types of drifts could be considered depending on the relative interaction between bottom currents, deposition, and faulting movement.

#### *Type-1*

Type-1 considers drifts to be deposited coeval to the fault movement, such as FD-1, -2, -5, and -6 (Table 2). Faulting movements are synchronous and continuous with the growth of this type of drifts, and two possibilities have been determined: a) Type-1a is a drift located over the footwall block of the normal fault. In this case, bottom currents circulated above the top part of the footwall block. Gravitational collapse can be triggered and slope-confined canyon can be formed on of the steep fault scarp (Fig. 10a). The drifts are characterized by irregular mounded geometry and moderate-high amplitude, as well as sigmoid to parallel reflections with onlap terminations. These deposits are disconnected from coeval

deposits which were deposited over the hanging wall block. b) The Type-1b drift extends from the footwall block to the hanging wall block and covers the normal fault plane. Bottom currents are focused along the middle part of the fault-generated scarp (Fig. 10b), forming a drift with slightly mounded geometry and moderate-high amplitude, as well as sigmoid reflections with onlap terminations. Progradational reflection configurations with onlap and downlap terminations could display over the fault footwall block.

#### *Type-2*

Type-2 considers drifts to be deposited after the fault movement, such as the FD-3 and FD-4 that are associated with moats (Table 2). The drifts occur via the interplay between the bottom currents and previously fault-generated seafloor relief (Fig. 10c). They are located along the base of the fault scarp where the bottom currents were locally enhanced. This drift type is internally characterized by mounded geometry and moderate-high amplitude, as well as sigmoid to parallel reflections with onlap and downlap terminations. Some overlap exists between these Type-2 fault-controlled drifts, elongated and mounded drifts, and infill drifts defined in the literature (see examples in Rebesco et al., 2014). Normal fault identification is the main criterion for distinguishing this type from others.

## **6. Conclusion**

The present study determines the common occurrence of fault-controlled contourite drifts in the southern South China Sea. These drifts show irregular mounded geometry and are associated with faults. Two major types are identified depending on their shapes, locations, and relative faulting movements: Type-1) drifts deposit coeval to the fault movement and are situated over the footwall block or along the fault scarp, and Type-2) drifts deposit after the fault movement and are located along the fault scarp base.

Fault-controlled drifts are a key element in deep-sea sedimentary systems with active tectonics. Their sedimentary record could allow for the decoding of the interplay between water mass circulation, sedimentary processes, geohazard, and recent tectonics. Therefore, this knowledge is of broad interest to geologists, oceanographers, and petroleum geologists. The present study reveals that new types of fault-controlled drifts exist that are not well studied in the literature and further detailed studies are required. Different morphologies of fault-controlled drifts are described based on normal fault relative movements, but future research should be conducted on other active tectonic settings (i.e., strike-slip faults, reverse

faults) for evaluating the distinct sedimentary stacking patterns, geometries, and evolution of drifts being controlled or affected by faults.

### **Acknowledgment**

This study was supported by the China Postdoctoral Science Foundation (grant number 2020TQ0369) and the National Natural Science Foundation of China (grant number 41976067). This study was conducted in collaboration with “The Drifters” Research Group of the Royal Holloway University of London (UK) and it is related to projects CTM 2012-39599-C03, CGL2016-80445-R, and CTM2016-75129-C3-1-R (REN2001-1734 C03-01/M). This study was carried out within the framework of the Geological Investigation Programs (No. DD20160155) of the China Geological Survey.

## Reference

- Boyer, T.P., J. I. Antonov, O. K. Baranova, C. Coleman, H. E. Garcia, A. Grodsky, D. R. Johnson, R. A. Locarnini, A. V. Mishonov, T.D. O'Brien, C.R. Paver, J.R. Reagan, D. Seidov, I. V. Smolyar, and M. M. Zweng, 2013: World Ocean Database 2013, NOAA Atlas NESDIS 72, S. Levitus, Ed., A. Mishonov, Technical Ed.; Silver Spring, MD, 209 pp. <http://doi.org/10.7289/V5NZ85MT>
- Cai, Z., Gan, J., Liu, Z., Hui, C.R., Li, J., 2020. Progress on the formation dynamics of the layered circulation in the South China Sea. *Prog. Oceanogr.* 181, 102246. <https://doi.org/10.1016/j.pocean.2019.102246>
- Ceramicola, S., Rebesco, M., De Batist, M., Khlystov, O., 2001. Seismic evidence of small-scale lacustrine drifts in Lake Baikal (Russia). *Mar. Geophys. Res.* 22, 445-464. <https://doi.org/10.1023/a:1016351700435>
- Chen, H., Xie, X., Zhang, W., Shu, Y., Wang, D., Vandorpe, T., Van Rooij, D., 2016. Deep-water sedimentary systems and their relationship with bottom currents at the intersection of Xisha Trough and Northwest Sub-Basin, South China Sea. *Mar. Geol.* 378, 101-113. <http://dx.doi.org/10.1016/j.margeo.2015.11.002>
- Cullen, A.B., 2010. Transverse segmentation of the Baram-Balabac Basin, NW Borneo: refining the model of Borneo's tectonic evolution. *Pet. Geosci.* 16, 3-29. <http://dx.doi.org/10.1144/1354-079309-828>
- Dugan, B., Flemings, P.B., 2000. Overpressure and Fluid Flow in the New Jersey Continental Slope: Implications for Slope Failure and Cold Seeps. *Science* 289, 288. <https://doi.org/10.1126/science.289.5477.288>
- Faugères, J.C., Stow, D.A.V., Imbert, P., Viana, A., 1999. Seismic features diagnostic of contourite drifts. *Mar. Geol.* 162, 1-38. [http://dx.doi.org/10.1016/S0025-3227\(99\)00068-7](http://dx.doi.org/10.1016/S0025-3227(99)00068-7)
- Faugères, J.C., Stow, D.A.V., 2008. Chapter 14 Contourite Drifts: Nature, Evolution and Controls, in: Rebesco, M., Camerlenghi, A. (Eds.), *Developments in Sedimentology*. Elsevier, pp. 257-288.
- Folk, R. L., Andrews, P. B., and Lewis, D. W., 1970. Detrital sedimentary rock classification and nomenclature for use in New Zealand. *New Zeal. J. Geol. Geop.* 13: 937-968. <https://doi.org/10.1080/00288306.1970.10418211>
- Fonnesu, M., Palermo, D., Galbiati, M., Marchesini, M., Bonamini, E., Bendias, D., 2020. A new world-class deep-water play-type, deposited by the syndepositional interaction of turbidity flows and bottom currents: The giant Eocene Coral Field in northern Mozambique. *Mar. Petrol. Geol.* 111, 179-201. <https://doi.org/10.1016/j.marpetgeo.2019.07.047>
- García, M., Hernández-Molina, F.J., Alonso, B., Vázquez, J.T., Ercilla, G., Llave, E., Casas, D., 2016. Erosive sub-circular depressions on the Guadalquivir Bank (Gulf of Cadiz): Interaction between bottom current, mass-wasting and tectonic processes. *Mar. Geol.* 378, 5-19. <https://doi.org/10.1016/j.margeo.2015.10.004>

- Hernández-Molina, F.J., Llave, E., Stow, D.A.V., 2008a. Chapter 19 Continental Slope Contourites, in: Rebesco, M., Camerlenghi, A. (Eds.), *Developments in Sedimentology*. Elsevier, pp. 379-408.
- Hernández-Molina, F.J., Maldonado, A., Stow, D.A.V., 2008b. Chapter 18 Abyssal Plain Contourites, in: Rebesco, M., Camerlenghi, A. (Eds.), *Developments in Sedimentology*. Elsevier, pp. 345-378.
- Hernández-Molina, F.J., Paterlini, M., Somoza, L., Violante, R., Arecco, M.A., de Isasi, M., Rebesco, M., Uenzelmann-Neben, G., Neben, S., Marshall, P., 2010. Giant mounded drifts in the Argentine Continental Margin: Origins, and global implications for the history of thermohaline circulation. *Mar. Petrol. Geol.* 27, 1508-1530. <https://doi.org/10.1016/j.marpetgeo.2010.04.003>
- Hernández-Molina, F.J., Paterlini, M., Violante, R., Marshall, P., de Isasi, M., Somoza, L., Rebesco, M., 2009. Contourite depositional system on the Argentine Slope: An exceptional record of the influence of Antarctic water masses. *Geology* 37, 507-510. <https://doi.org/10.1130/g25578a.1>
- Hernández-Molina, F.J., Stow, D.A.V., Alvarez-Zarikian, C.A., Actor, G., Bair, A., Balestra, B., Ducassou, E., Flood, R., Flores, J.-A., Furota, S., Grunert, P., Hodell, D., Jimenez-Espejo, F., Kim, J.K., Krissek, L., Kuroda, J., Li, B., Llave, E., Lofi, J., Lourens, L., Miller, M., Nanayama, F., Nishida, N., Richter, C., Roque, C., Pereira, H., Sanchez Goñi, M.F., Sierro, F.J., Singh, A.D., Sloss, C., Takahamizu, Y., Tzanova, A., Voelker, A., Williams, T., Xuan, C., 2014. Onset of Mediterranean outflow into the North Atlantic. *Science* 344, 1244-1250. <https://doi.org/10.1126/science.1251306>
- Hutchison, C.S., 2004. Marginal basin evolution in the southern South China Sea. *Mar. Petrol. Geol.* 21, 1129-1148. <https://doi.org/10.1016/j.marpetgeo.2004.07.002>
- Jones, E.J.W., Okada, H., 2006. Abyssal circulation change in the equatorial Atlantic: Evidence from Cenozoic sedimentary drifts of West Africa. *Mar. Geol.* 232, 49-61. <https://doi.org/10.1016/j.margeo.2006.07.002>
- Kuhlbrodt, T., Griesel, A., Montoya, M., Levermann, A., Hofmann, M., Rahmstorf, S., 2007. On the driving processes of the Atlantic meridional overturning circulation. *Rev. Geophys.* 45, RG2001. <https://doi.org/10.1029/2004RG000166>
- Laberg, J.S., Camerlenghi, A., 2008. Chapter 25 The Significance of Contourites for Submarine Slope Stability, in: Rebesco, M., Camerlenghi, A. (Eds.), *Developments in Sedimentology*. Elsevier, pp. 537-556.
- Levchenko, O.V., Putans, V.A., Borisov, D.G., 2018. Contourites in the Derbent Basin, Caspian Sea (Geophysical Data). *Dokl. Earth Sci.* 482, 1239-1243. <https://doi.org/10.1134/S1028334X18090258>
- Liang, C., Xie, X.-N., Wang, H., Chen, H., Shi, G.-Z., Zhong, G.-J., Liu, E.-T., Sun, M., Yi, H., 2019. Depositional evolution of sediment drifts inside intra-slope basins on the lower southeastern slope of the Dongsha Islands (South

- China Sea) and their paleoceanographic implications. *Geo-Mar. Lett.* 39, 101-116. <https://doi.org/10.1007/s00367-019-00561-7>
- Liu, S., Van Rooij, D., Vandorpe, T., González-Pola, C., Ercilla, G., Hernández-Molina, F.J., 2019. Morphological features and associated bottom-current dynamics in the Le Danois Bank region (southern Bay of Biscay, NE Atlantic): A model in a topographically constrained small basin. *Deep Sea Res. Part I Oceanogr. Res. Pap.* 149, 103054. <https://doi.org/10.1016/j.dsr.2019.05.014>
- Llave, E., Hernández-Molina, F.J., García, M., Ercilla, G., Roque, C., Juan, C., Mena, A., Preu, B., Van Rooij, D., Rebesco, M., Brackenridge, R., Jané, G., Gómez-Ballesteros, M., Stow, D., 2019. Contourites along the Iberian continental margins: conceptual and economic implications. *Geological Society, London, Special Publications* 476, 403-436. <https://doi.org/10.1144/SP476-2017-46>
- Madon, M., Kim, C.L., Wong, R., 2013. The structure and stratigraphy of deepwater Sarawak, Malaysia: Implications for tectonic evolution. *J. Asian. Earth. Sci.* 76, 312-333. <https://doi.org/10.1016/j.jseaes.2013.04.040>
- Maldonado, A., Barnolas, A., Bohoyo, F., Escutia, C., Galindo-Zaldívar, J., Hernández-Molina, J., Jabaloy, A., Lobo, F.J., Nelson, C.H., Rodríguez-Fernández, J., Somoza, L., Trápanez, J.-T., 2005. Miocene to Recent contourite drifts development in the northern Weddell Sea. *Global. Planet. Change.* 45, 99-129. <http://dx.doi.org/10.1016/j.gloplacha.2004.09.013>
- Martins, L.R., 2003. Recent Sediments and Grain-Size Analysis. *Sedimentological Research Group e SERG/ASOS, Gravel 1, Porto Alegre*, pp. 90-105.
- McHugh, C.M.G., Damuth, J.E., Mountain, G.S., 2002. Cenozoic mass-transport facies and their correlation with relative sea-level change, New Jersey continental margin. *Mar. Geol.* 184, 295-334. [https://doi.org/10.1016/S0025-3227\(01\)00240-7](https://doi.org/10.1016/S0025-3227(01)00240-7)
- McManus, J., 1988. Grain size determination and interpretation. In: Tuck, M., E., (Eds.), *Techniques in Sedimentology*. Blackwell Scientific Publications, Tucker. p.63–85.
- Miramontes, E., Garreau, P., Caillaud, M., Jouet, G., Pellen, R., Hernández-Molina, F.J., Clare, M.A., Cattaneo, A., 2019. Contourite distribution and bottom currents in the NW Mediterranean Sea: Coupling seafloor geomorphology and hydrodynamic modelling. *Geomorphology* 333, 43-60. <https://doi.org/10.1016/j.geomorph.2019.02.030>
- Miramontes, E., Eggenhuisen, J.T., Jacinto, R.S., Poneti, G., Pohl, F., Normandeau, A., Campbell, D.C., Hernández-Molina, F.J., 2020. Channel-levee evolution in combined contour current–turbidity current flows from flume-tank experiments. *Geology* 48, 353-357. <https://doi.org/10.1130/G47111.1>

- Mulder, T., Ducassou, E., Hanquiez, V., Principaud, M., Fauquembergue, K., Tournadour, E., Chabaud, L., Reijmer, J., Recouvreur, A., Gillet, H., Borgomano, J., Schmitt, A., Moal, P., 2019. Contour current imprints and contourite drifts in the Bahamian archipelago. *Sedimentology* 66, 1192-1221. <https://doi.org/10.1111/sed.12587>
- Palamenghi, L., Keil, H., Spiess, V., 2015. Sequence stratigraphic framework of a mixed turbidite-contourite depositional system along the NW slope of the South China Sea. *Geo-Mar. Lett.* 35, 1-21. <https://doi.org/10.1007/s00367-014-0385-z>
- Pratson, L.F., Coakley, B.J., 1996. A model for the headward erosion of submarine canyons induced by downslope-eroding sediment flows. *GSA Bull.* 108, 225-234. [https://doi.org/10.1130/0016-7606\(1996\)108<0225:AMFTHE>2.3.CO;2](https://doi.org/10.1130/0016-7606(1996)108<0225:AMFTHE>2.3.CO;2)
- Preu, B., Schwenk, T., Hernández-Molina, F.J., Violante, R., Paterlini, M., Krastse, S., Tomasini, J., Spieß, V., 2012. Sedimentary growth pattern on the northern Argentine slope: The impact of North Atlantic Deep Water on southern hemisphere slope architecture. *Mar. Geol.* 329-331, 113-125. <https://doi.org/10.1016/j.margeo.2012.09.009>
- Qu, T., Girton, J.B., Whitehead, J.A., 2006. Deepwater overflows through Luzon Strait. *J. Geophys. Res. Oceans.* 111, C01002. <http://dx.doi.org/10.1029/2005JC003152>
- Rebesco, M., Stow, D.A.V., 2001. Seismic expression of contourites and related deposits: a preface. *Mar. Geophys. Res.* 22, 303-308. <http://dx.doi.org/10.1023/A:1016316913639>
- Rebesco, M., 2005. Contourites. In: Selley, R.C., Cocks, L.R.M., Plimer, I.R. (Eds.), *Encyclopedia of Geology*. Elsevier, Oxford, pp. 513-527.
- Rebesco, M., Hernández-Molina, F.J., Van Rooij, D., Wählin, A., 2014. Contourites and associated sediments controlled by deep-water circulation processes: State-of-the-art and future considerations. *Mar. Geol.* 352, 111-154. <http://dx.doi.org/10.1016/j.margeo.2014.03.011>
- Roque, C., Duarte, H., Terrinha, P., Valadares, V., Noiva, J., Cachão, M., Ferreira, J., Legoinha, P., Zitellini, N., 2012. Pliocene and Quaternary depositional model of the Algarve margin contourite drifts (Gulf of Cadiz, SW Iberia): Seismic architecture, tectonic control and paleoceanographic insights. *Mar. Geol.* 303-306, 42-62. <http://dx.doi.org/10.1016/j.margeo.2011.11.001>
- Sansom, P., 2018. Hybrid turbidite-contourite systems of the Tanzanian margin. *Pet. Geosci.* 24, 258-276. <https://doi.org/10.1144/petgeo2018-044>



- Shu, Y., Xue, H., Wang, D., Chai, F., Xie, Q., Cai, S., Chen, R., Chen, J., Li, J., He, Y., 2016. Persistent and energetic bottom-trapped topographic Rossby waves observed in the southern South China Sea. *Sci. Rep.* 6, 24338. <https://doi.org/10.1038/srep24338>
- Sibuet, J.-C., Yeh, Y.-C., Lee, C.-S., 2016. Geodynamics of the South China Sea. *Tectonophysics* 692, 98-119. <https://doi.org/10.1016/j.tecto.2016.02.022>
- Solheim, A., Bryn, P., Sejrup, H.P., Mienert, J., Berg, K., 2005. Ormen Lange—an integrated study for the safe development of a deep-water gas field within the Storegga Slide Complex, NE Atlantic continental margin; executive summary, in: Solheim, A., Bryn, P., Berg, K., Sejrup, H.P., Mienert, J. (Eds.), *Ormen Lange—an Integrated Study for Safe Field Development in the Storegga Submarine Area*. Elsevier, Oxford, pp. 1-9.
- Stanley, D.J., 1993. Model for turbidite-to-contourite continuum and multiple process transport in deep marine settings: examples in the rock record. *Sediment. Geol.* 82, 241-255. [https://doi.org/10.1016/0037-0738\(93\)90124-N](https://doi.org/10.1016/0037-0738(93)90124-N)
- Stow, D.A.V., Faugères, J.-C., Howe, J.A., Pudsey, C.J., Viana, A.R., 2002. Bottom currents, contourites and deep-sea sediment drifts: current state-of-the-art. *Geological Society, London, Memoirs* 22, 7-20. <https://doi.org/10.1144/gsl.mem.2002.022.01.02>
- Stow, D.A.V., Javier Hernández-Molina, F., Llave, E., Saiz, M., 2009. Bedform-velocity matrix: The estimation of bottom current velocity from bedform observations. *Geology* 37, 327-330. <https://doi.org/10.1130/G25259A1>
- Stow, D.A.V., Hernández-Molina, F.J., Llave, E., Bruno, M., García, M., Díaz del Río, V., Somoza, L., Brackenridge, R.E., 2013. The Cadiz Contourite Channel: Sandy contourites, bedforms and dynamic current interaction. *Mar. Geol.* 343, 99-114. <https://doi.org/10.1016/j.margeo.2013.06.013>
- Su, J., 2004. Overview of the South China Sea circulation and its influence on the coastal physical oceanography near the Pearl River Estuary. *Cont. Shelf. Res.* 24, 1745-1760. <https://doi.org/10.1016/j.csr.2004.06.005>
- Tian, J., Ma, X., Zhou, J., Wang, W., 2017. Subsidence of the northern South China Sea and formation of the Bashi Strait in the latest Miocene: Paleoceanographic evidences from 9-Myr high resolution benthic foraminiferal  $\delta^{18}\text{O}$  and  $\delta^{13}\text{C}$  records. *Palaeogeogr. Palaeoclimatol. Palaeoecol.* 466, 382-391. <https://doi.org/10.1016/j.palaeo.2016.11.041>
- Tian, J., Yang, Q., Liang, X., Xie, L., Hu, D., Wang, F., Qu, T., 2006. Observation of Luzon Strait transport. *Geophys. Res. Lett.* 33. <https://doi.org/10.1029/2006GL026272>

- Turnewitsch, R., Falahat, S., Nycander, J., Dale, A., Scott, R.B., Furnival, D., 2013. Deep-sea fluid and sediment dynamics—Influence of hill- to seamount-scale seafloor topography. *Earth. Sci. Rev.* 127, 203-241. <https://doi.org/10.1016/j.earscirev.2013.10.005>
- Turnewitsch, R., Reyss, J.-L., Chapman, D.C., Thomson, J., Lampitt, R.S., 2004. Evidence for a sedimentary fingerprint of an asymmetric flow field surrounding a short seamount. *Earth Planet. Sci. Lett.* 222, 1023-1036. <https://doi.org/10.1016/j.epsl.2004.03.042>
- Wang, D., Xiao, J., Shu, Y., Xie, Q., Chen, J., Wang, Q., 2016. Progress on deep circulation and meridional overturning circulation in the South China Sea. *Sci. China Earth Sci.* 59, 1827-1833. <https://doi.org/10.1007/s11430-016-5324-6>
- Wentworth, C.K., 1922. A scale of grade and class terms for classic sediments. *J. Geol.* 30: 377-392. <https://doi.org/10.1086/622910>
- Wunsch, C., 2002. What Is the Thermohaline Circulation? *Science* 298, 1179. <https://doi.org/10.1126/science.1079329>
- Xiao, J., Xie, Q., Liu, C., Chen, J., Wang, D., Chen, M., 2013. A diagnostic model of the South China Sea bottom circulation in consideration of tidal mixing, eddy-induced mixing and topography. *Hai. Yang. Xue. Bao.* 35, 1-13.
- Xie, Q., Xiao, J., Wang, D., Yu, Y., 2013. Analysis of deep-layer and bottom circulations in the South China Sea based on eight quasi-global ocean model outputs. *Chin. Sci. Bull.* 58, 4000-4011.
- Yin, S., Hernández-Molina, F.J., Zhang, W., Li, J., Wang, L., Ding, W., Ding, W., 2019. The influence of oceanographic processes on contourite features: A multidisciplinary study of the northern South China Sea. *Mar. Geol.* 415, 105967. <https://doi.org/10.1016/j.margeo.2019.105967>
- Zhang, L., Wang, L., Yi, H., 2003. The formation and evolution of Beikang Basin. *China Offshore Oil and Gas* 17, 245-248.
- Zhang, J., Li, A., Wan, S., Huang, J., Lu, J., Jiang, F., Li, T., 2016. Grain size distribution of surface sediments in the southern South China Sea and influencing factors. *Mar. Geol. & Quat. Geol.* 36, 1-10.
- Zhou, C., Zhao, W., Tian, J., Zhao, X., Zhu, Y., Yang, Q., Qu, T., 2017. Deep Western Boundary Current in the South China Sea. *Sci. Rep.* 7, 9303. <https://doi.org/10.1038/s41598-017-09436-2>

## Figures

**Fig. 1.** a) Regional map indicating the location of the southern South China Sea (SCS) and the regional circulation of the Surface (SW), the Intermediate (IW), Deep (DW), and Bottom (BW) water masses (adapted from Tian et al., 2006). b) Morphological map (contour lines every 200 m) of the southern SCS, including the study area (red dot box).

**Fig. 2.** High-resolution bathymetric map with indications of the main regional geographic and morphological features.

**Fig. 3.** a) Mean velocities of the bottom currents at a water depth of 2000 m in the SCS (modified from Xiao et al., 2013); b) Vertical water column near the Luzon Strait indicating the flow velocity (cm/s). Positive velocity values denote eastward flow while negative values denote westward flow (Tian et al., 2006); c) Potential temperature versus salinity diagram from the water masses in the study area (World Ocean Database, 2013); d) Oceanographic cross-section of the study area indicating the occurrence of the SCS DW in the study area. The water column colour ranges indicate salinity. CTD stations (red triangles) and their respective locations are indicated in the cross-section profile. The location of this profile is shown in Fig. 1a and Fig. 1b. SW= the South China Sea Surface Water; IW=the South China Sea Intermediate Water; DW=the South China Sea Deep Water; BW=the South China Sea Bottom Water.

**Fig. 4.** a) Dataset map indicating the locations of seismic profiles and the well Bako-1, as well as the surface sediment cores from Zhang et al. (2016); b) Three seismic units (units 3, 2, and 1) and major discontinuities (horizons T3, T2, and T1) from the bottom to the top; c) Seismic stratigraphic framework of the Beikang Basin. Timing of major unconformities is compared with previous studies from Madon et al. (2013) and borehole well Bako-1.

**Fig. 5.** a) Present-day regional morphosedimentary map of the study area indicating the occurrence of main depositional and erosional features, including the studied fault-controlled drifts; b) Slope map (in degrees) of the study area.

**Fig. 6.** Seismic profiles and their interpretation, showing fault-controlled drifts (FD) 1 and 2 and their internal structures. Seismic terminations are indicated by violet arrows. The location of these seismic lines is displayed in Fig. 4. T3=the Early Miocene Unconformity (16 Ma; dark blue dotted

line); T2=the Late Miocene Unconformity (5.5 Ma; green dotted line); T1=the Early Quaternary Unconformity (2 Ma; red dotted line).

**Fig. 7.** Seismic profiles and their interpretation, indicating fault-controlled drifts (FD) 3 and 4, and their internal structures. Seismic terminations are indicated by violet arrows. The location of these seismic lines is displayed in Fig. 4. T3=the Early Miocene Unconformity (16 Ma; dark blue dotted line); T2=the Late Miocene Unconformity (5.5 Ma; green dotted line); T1=the Early Quaternary Unconformity (2 Ma; red dotted line).

**Fig. 8.** (a) High-resolution bathymetry map with the location of the displayed seismic profiles for the area with fault-controlled drifts (FD) 5 and 6. The location of the area is indicated in Fig. 4; (b, c, d, e, f) Seismic profiles and their interpretation, illustrating FD-5 and FD-6, elongated and mounded drifts, submarine canyons, and background hemipelagic deposits. Seismic terminations are indicated by violet arrows. T3=the Early Miocene Unconformity (16 Ma; dark blue dotted line); T2=the Late Miocene Unconformity (5.5 Ma; green dotted line); T1=the Early Quaternary Unconformity (2 Ma; red dotted line).

**Fig. 9.** Variations of grain size and the content of clay and silt along the latitude east of 112.5° E (modified from Zhang et al., 2016). The locations of selected surface sediment cores are indicated in Fig. 4a.

**Fig. 10.** 3D schematics showing two main types of fault-controlled drifts: Type-1) drifts deposited coeval to the fault movement and are situated over the footwall block (Type-1a) or along the fault scarp (Type-1b), and Type-2) drifts deposited after the fault movement and are located along the fault scarp base. Bottom-current pathways are indicated. Red arrows indicate bottom currents while blue arrows represent gravity flows.

**Table 1.** Description and examples of seismic facies of depositional features.

**Table 2.** Fault-controlled drift characteristics and associated fault-contourite interactions.

**Declaration of interests**

The authors declare that they have no known competing financial interests or personal relationships that could have appeared to influence the work reported in this paper.

The authors declare the following financial interests/personal relationships which may be considered as potential competing interests:

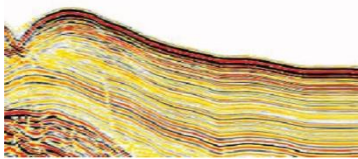
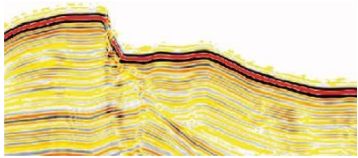
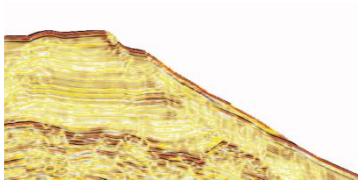
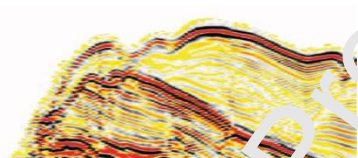
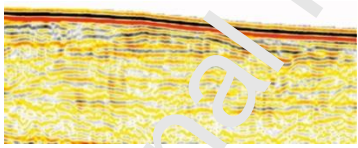

Journal Pre-proof

### Highlights

- Fault-controlled drifts are a key element in deep-sea sedimentary systems.
- Regional faulting movements have been active from the Quaternary to the present day.
- Two types of fault-controlled contourite drifts are classified.
- Interactions between the bottom currents and gravity flows occur at the fault scarp.
- The South China Sea Deep Water upwells in the southern South China Sea.

Journal Pre-proof

**Table 1.** Description and examples of seismic facies of depositional features.

depositional type	seismic expression	Seismic facies
elongated and mounded drift		moderate-high amplitude; continuous oblique to subparallel reflections with onlap terminations; mounded geometry
fault-controlled drift		moderate-high amplitude; continuous oblique to subparallel reflections; mounded features with onlap terminations towards the lower part of the fault plain
		moderate-high amplitude; sigmoid reflections; slightly mounded geometry; onlap terminations over the entire fault plane
		moderate-high amplitude; sigmoid to parallel reflections with onlap terminations; irregular mounded geometry
mass-transport deposit		low-moderate amplitude, transparent to chaotic reflections
pelagic/hemipelagic deposit		moderate-high amplitude; continuous parallel reflections

**Table 2.** Fault-controlled drift characteristics and associated fault-contourite interactions.

<b>fault-controlled drift</b>	<b>depth (m)</b>	<b>size (km<sup>2</sup>)</b>	<b>slope gradient</b>	<b>geometry</b>	<b>fault-contourite interaction</b>	<b>type</b>
FD-1	1470-1910	21	7° -13°	slightly mounded	generated coeval to faulting movement	Type-1b
FD-2	1290-1660	40	14°-28°	irregularly mounded	generated coeval to faulting movement	Type-1a
FD-3	1230-1480	74	7°-15°	mounded	generated after faulting movement	Type-2
FD-4	1420-1810	107	9°-17°	mounded	generated after faulting movement	Type-2
FD-5	1380-2040	32	6°-10°	irregularly mounded	generated coeval to faulting movement	Type-1a
FD-6	1190-1630	40	15° -28°	slightly mounded	generated coeval to faulting movement	Type-1b

table 2